Impact of Moisture on efficiency-determining electronic processes in Perovskite Solar Cells

Manuel Salado[a,b], Lidia Contreras-Bernal[a], Anna Todinova[a], Carmen Lopez-Santos[c], Laura Caliò[b], Shahzada Ahmad[b], Ana Borras[c], Jesús Idígoras[a,*], Juan A. Anta[a,*].

[a] *Área de Química Física, Universidad Pablo de Olavide, E-41013, Sevilla, Spain.*

[b] *Abengoa Research, C/Energía Solar n° 1, Campus Palmas Altas, 41014 Sevilla, Spain*

[c] *Nanotechnology on Surfaces Laboratory, Instituto de Ciencia de Materiales de Sevilla (CSIC-Univ. Sevilla), Seville ES-41092, Spain*

ABSTRACT

The moisture-induced degradation in perovskite solar cells is thoroughly investigated by materials (SEM, EDX, XRD) and device characterization (impedance and intensity modulated photocurrent spectroscopies). Both the influence of the perovskite composition and the nature of the hole selective material were analyzed. The degradation rate is found to be significantly slower for mixed perovskites and P3HT-based devices. However, for a fixed degradation degree (defined as a 50% drop of the initial photocurrent), all configurations show similar features in the small-perturbation analysis. Thus, a new mid-frequency signal appears in the impedance response, which seems to be related to charge accumulation at the interfaces. In addition, faster recombination, with a more important surface contribution, and slower transport is clearly inferred from our results. Both features can be associated with the deterioration of the contacts and the formation of a greater number of grain boundaries.

INTRODUCTION

Over the last decades, the research community has paid special interest to the development of advanced, efficient and low-cost photovoltaic technologies. In this context, hybrid organic-inorganic metal halide perovskite materials have attracted much attention owing to their excellent optoelectronic properties.[1–5] As a result, since the first report of the perovskite material as sensitizer in dye-sensitize solar cells (η = 3.8%),[6] a significant improvement of photovoltaic conversion efficiency has been achieved with a current

efficiency record of η = 21.1%[7] for full perovskite solar cell devices. This figure is comparable to photovoltaic performances of other thin-film photovoltaic technologies based on Si, CdTe and GaAs. This remarkable development was possible due to intensive research focused on device-engineering and material design.[8–12] However, in spite of this progress, the lack of a long-term stability restricts its outdoor photovoltaic applications[13] and as a consequence its commercialization.

It is well-known that the stability of perovskite solar cells (PSCs) and therefore their photovoltaic performance are intimately associated to the degradation of perovskite layer. As it was previously reported, the main causes behind perovskite degradation are related to different environmental factors,[14–16] such as moisture, temperature, oxygen and UV light, which could give rise to different degradation pathways. For instance, Niu et al. suggested that the perovskite degradation starts with the deprotonation of the methylammonium cation by water to produce methylamine, hydrogen iodide and lead iodide.[17] Yang et al. proposed the formation of colorless hydrated $(CH_3NH_3)_4PbI_6 \cdot 2H_2O$ as a result of perovskite hydration and the formation of lead iodide as final product.[18] Haque et al. described the perovskite degradation by the coupled effect of molecular oxygen and light suggesting that reactive oxygen species and the organic cation of perovskite react among themselves.[19] In any case, many approaches have been developed in order to prevent the perovskite degradation and guarantee the device stability. Among them stand out the effective passivation of devices by the use of hydrophobic polymers layers, the employment of photopolymerized fluorinated coatings, hydrophobic hole-selective materials, hydrophobic carbon electrodes and a thin blocking layer between perovskite and electron-selective layers.[20–25]

Nevertheless, the impact of these environmental factors on perovskite degradation kinetics depends on other intrinsic properties such as thermal and electrical stability, which is determined by the perovskite composition. Hybrid organic-inorganic metal halide perovskites are defined by the chemical formula ABX_3, where A is an organic or inorganic cation (MA = $CH_3NH_3^+$, FA = $HC(NH_2)_2^+$, Cs^+), B is a metal (Pb, Sn) and X is a halide (I⁻, Br⁻, Cl⁻). The chemical nature of these elements does not only influence the photoelectronic behavior, but also the structural properties defined by the tolerance factor (t)[26]

$$t = \frac{(r_A + r_X)}{\left(\sqrt{2}(r_B + r_X)\right)}$$

where r_A, r_B and r_X are the ionic radii of the different elements A, B and X, respectively. Empirically, for the most stable perovskite, t shows values between 0.8 and 1 giving rise to cubic crystal structure. However, for t < 0.8 the tetragonal or orthorhombic crystal structure are more probable.[26,27] As a consequence, special attention has been paid to the perovskite composition in order to achieve a more stable crystal structure and guarantee a long-term stability by the entire or partial inclusion of different ions with different sizes. For instance, it has been demonstrated the beneficial effect in terms of stability of a partial insertion of bromine into the perovskite structure.[28,29] Similar results were found for the inclusion of chloride.[30] In the both cases, the smaller ionic radii of Br and Cl with respect to I leads to a more compact structure in which the organic cations are less exposed. More recently, Petrus

and coworkers reported the impact of the excess of PbI_2 as precursor on perovskite stability against moisture exposure.[31] In relation to the organic cations, t values of 0.88 and 0.83 were found for perovskites containing MA and FA, respectively.[32] The higher thermal stability found for $FAPbI_3$ was associated with the more-stable cubic crystal phase with respect to the tetragonal one attributed to $MAPbI_3$, which could be related to the different interaction of these cations with the inorganic matrix.[27] Similar results were found by Snaith et al. when they compared $CsPbI_2Br$ and $MAPbI_2Br$ and demonstrated the stability of the former owing to the appropriate ionic radii of Cs^+.[33] More recently, the stability of triple cation perovskite (MA, FA and Cs) has also been investigated.[34]

Up to the date, previous studies related to the perovskite stability have mainly investigated the different perovskite degradation mechanisms under environmental factors or different approaches to prevent the perovskite degradation. SEM and STEM images, EDS mapping, UV-Vis absorbance, XRD diffraction patterns, Raman and IR spectroscopy have been techniques commonly used to characterize the extent of perovskite degradation and its kinetics. However, to the best our knowledge, this is the first report where small-perturbation optoelectronic techniques have been used to investigate the impact of moisture on the electronic processes that determine the photovoltaic performance. This is important to better assess how the perovskite improvements investigated in the literature really affect the functioning of the device in terms of stability and efficiency. In order to correlate the moisture effect on this, we have analyzed the electron transport and recombination processes using impedance spectroscopy (IS) and intensity-modulated photocurrent spectroscopy (IMPS). In this work, we have investigated both the influence of the perovskite composition ($MAPbI_3$ = *MAI* and $Cs_{0.05}(MAPbBr_3)_{0.15}(FAPbI_3)_{0.85}$ = *MIX*) and the influence of the hole selective material (*HSL*: 2,2´,7,7´-Tetrakis(N,N-di-p-methoxyphenylamine)-9,9´-spirobifluorene = *Spiro-OMeTAD* and poly(3-hexylthiophene-2,5-diyl) = *P3HT*) on the device stability. In particular, a faster degradation rate was found for *MAI* perovskite and Spiro-based devices. Regardless of the device configuration, our results point to a faster recombination after moisture exposure due to the coupled effect of the bulk recombination and the surface-mediated recombination. The greater contribution of the latter in degraded devices is revealed by interfacial charge accumulation processes and slower electron transport inside the perovskite layer.

EXPERIMENTAL SECTION

Fabrication of Perovskite Solar Cells

Perovskite solar cells devices were fabricated on FTO-coated glass (Pilkington–TEC15) patterned by laser etching. Prior to use, the substrates were cleaned using Hellmanex® solution and rinsed with deionized water and ethanol. Followed this they were ultrasonicated in acetone, rinsed using 2-propanol and dried by using compressed air. TiO_2 compact layer was deposited by spray pyrolysis at 450ºC using titanium diisopropoxide bis(acetylacetonate) precursor solution (75% in 2-propanol, Sigma Aldrich) using O_2 as a carrier gas. The TiO_2 blocking layer was then annealed for further 30 minutes at 450 ºC for the formation of anatase phase. Once the samples achieve room temperature, a TiO_2 mesoporous layer (Dyesol, 30NRD) was deposited by spin coating (4000 rpm for 30 s) and the samples were annealed at 450 ºC. Subsequently, pure methylammonium ($MAPbI_3$ = *MAI*) or mixed cation perovskite ($Cs_{0.05}(MAPbBr_3)_{0.15}(FAPbI_3)_{0.85}$ = *MIX*) was then deposited

(see the Supporting Information, Figure S1). Pure methylammonium perovskite precursor solution was prepared mixing 1.2M MAI and PbI_2 (1:1.15) in DMSO. Mixed cation perovskite were prepared by dissolving FAI (1.01M), MABr (0.20M), PbI_2 (1.21M) and $PbBr_2$ (0.20M) in a mixture of solvents DMSO/DMF (1:4, v/v). After that, CsI (5 wt %) were added (from a stock solution 1.5M in DMSO) to the precursor solution. The perovskite solution was spin coated in a two steps setup at 1000 and 6000 rpm for 10 and 20s respectively. During the second step, 110μL of chlorobenzene was dropped on the spinning substrate 15 seconds before the end of the spinning program. The samples were then annealed (100°C) for 1h in an Argon filled glove box. Later perovskite deposition, 35 μL of a Spiro-OMeTAD or P3HT solution was then spin coated at 4000 rpm for 20 seconds as hole transporting material. Spiro-OMeTAD material (70mM) were dissolved in 1 mL of chlorobenzene using standard additives as 17.5 μL of a lithium bis(trifluoromethylsulphonyl)imide (LiTFSI) stock solution (520 mg of LiTFSI in 1mL of acetonitrile), 21.9 μL of a FK209 (Tris(2-(1H-pyrazol-1-yl)-4-tert-butylpyridine)cobalt(III)Tris(bis(trifluoromethylsulfonyl)imide))) stock solution (400 mg in 1 mL of acetonitrile) and 28.8 μL of 4-tert-butylpyridine (t-BP). In the case of P3HT material, 15 mg/mL solution in chlorobenzene was prepared and doped with 6.8ml of a 28.3 mg/mL stock solution of LiTFSI in acetonitrile. Finally, 80 nm of gold was deposited by thermal evaporation under a vacuum level between $1\cdot10^{-6}$ and $1\cdot10^{-5}$ torr. All solutions were prepared inside an argon glove box under controlled moisture and oxygen conditions (H_2O level: <1 ppm and O_2 level: <10 ppm). For simplicity we will use the following notation to refer to the different device configurations studied: *MAI/Spiro*, *MAI/P3HT*, *MIX/Spiro* and *MIX/P3HT*

Characterization of films and devices

The devices were characterized using current-voltage characteristics by two different light sources: (1) a solar simulator (ABET-Sun2000) under 100mW/cm² illumination with AM 1.5G filter and (2) a white light emitting diode (LED, LUXEON). The light intensity was recorded using a reference solar cell with temperature output (Oriel, 91150). The current-voltage characteristics were determined by applying an external potential bias to the cell and measuring the photocurrent using an Autolab/PGSTAT302N potentiostat.

The illumination for the different Impedance Spectroscopy (IS) measurements was provided by white, red and blue LEDs (λ_{blue} = 465 nm and λ_{red} = 635 nm) over a wide range of DC light intensities. This allows for probing the devices at different positions of the Fermi level in the semiconductor and for different optical generation profiles. COLOR PAPER A response analyzer module (PGSTAT302N/FRA2, Autolab) was utilized to analyze the frequency response of the devices. To avoid voltage drop due to series resistance, IS measurements were performed at the open circuit potential, the Fermi level (related to the open-circuit voltage) being fixed by the DC illumination intensity. A 20 mV perturbation in the 10^6-10^{-2} Hz range was utilized to obtain the spectra. IMPS measurements were performed at short-circuit in the 10^6 to 10^{-2}Hz range with a light perturbation corresponding to 10% of the DC background illumination intensity. To avoid any additional degradation process related to the moisture, the measurements were carried out under N_2-atmosphere. The NOVA 1.7 software was used to generate IS data. Z-view equivalent circuit modeling software (Scribner) was used to fit the spectra.

For the structural characterization, perovskite films were prepared by spin coating onto Si wafers. Scanning electron microscope (SEM) images of the samples were performed using a Zeiss GeminiSEM-300 microscope working at 2KeV. Electron Backscatter Diffraction (EBSD) images were obtained using NordlysMax3 detector (Oxford Instruments). Energy Dispersive Spectroscopy (EDS) was performed using a Silicon Drift Detector (Oxford Instruments). X-ray diffractograms were recorded on a Rigaku diffractometer using CuKα source. The measurements were performed at grazing angle geometry. The samples were mounted without any further modification and the divergence slit were adjusted to the dimension of the films. A scan range from 10° to 60° was selected with an acquisition time of 3 degree/min. A baseline correction was applied to the diffractograms to compensate for the noise arising from the substrate. X-Ray Photoelectron Spectroscopy (XPS) characterization was performed in a Phoibos 100 DLD X-ray spectrometer from SPECS. The spectra were collected in the pass energy constant mode at a value of 50 eV for the general spectra and 30 eV for the different peaks using a Mg Kα source. C1s signal at 284.5 eV was utilized for calibration of the binding energy in the spectra. Static water contact angle (WCA) measurements were provided by a Data Physics setup by depositing bidistilled water drops of 1μL. The given values correspond to a statistics over 10 values. The WCAs were evaluated for pinning droplets several seconds after the contact with the surfaces.

RESULTS AND DISCUSSION

Power conversion efficiencies in the range 12-16% were obtained under standard conditions (1 sun - AM 1.5 illumination) for the different PSCs studied (Figure S2). Current-Voltage characteristics of the different PSCs were measured in reverse scan (from open-circuit condition to short-circuit condition) at a scan rate of 100mV·s^{-1} with a waiting time of 30 s at 1.2V. In particular, average efficiencies of 15.3%, 13.2%, 13% and 12.5% were obtained for MAI/Spiro, MAI/P3HT, MIX/Spiro and MIX/P3HT devices, respectively (see Supporting Information, Table S1[BMAI1]). In line with the literature,[35–37] these results highlight the impact of the perovskite composition and the material used as HSL on the photovoltaic performance. For both perovskite compositions, better efficiencies were found when Spiro-OMeTAD was used as HSL with respect to P3HT as a result of the higher V_{OC}. Additionally, in spite of showing similar J_{SC} and V_{OC} for the both HSL, worse efficiencies were obtained for MIX devices due to its lower fill factor. These different devices will be used for the following discussion.

In order to investigate the impact of the moisture exposure [BMAI2]on the device stability, the photovoltaic performance of the different PSCs were measured inside a hermetic chamber-holder with a constant flow of air with a RH > 90%. Figure 1 shows current-voltage characteristics of PSCs measured by cyclic voltammetry before and during the moisture exposure. The measurements were started with a reverse scan after a poling of 10 s at 1.2 V, and were then continued with a forward scan.
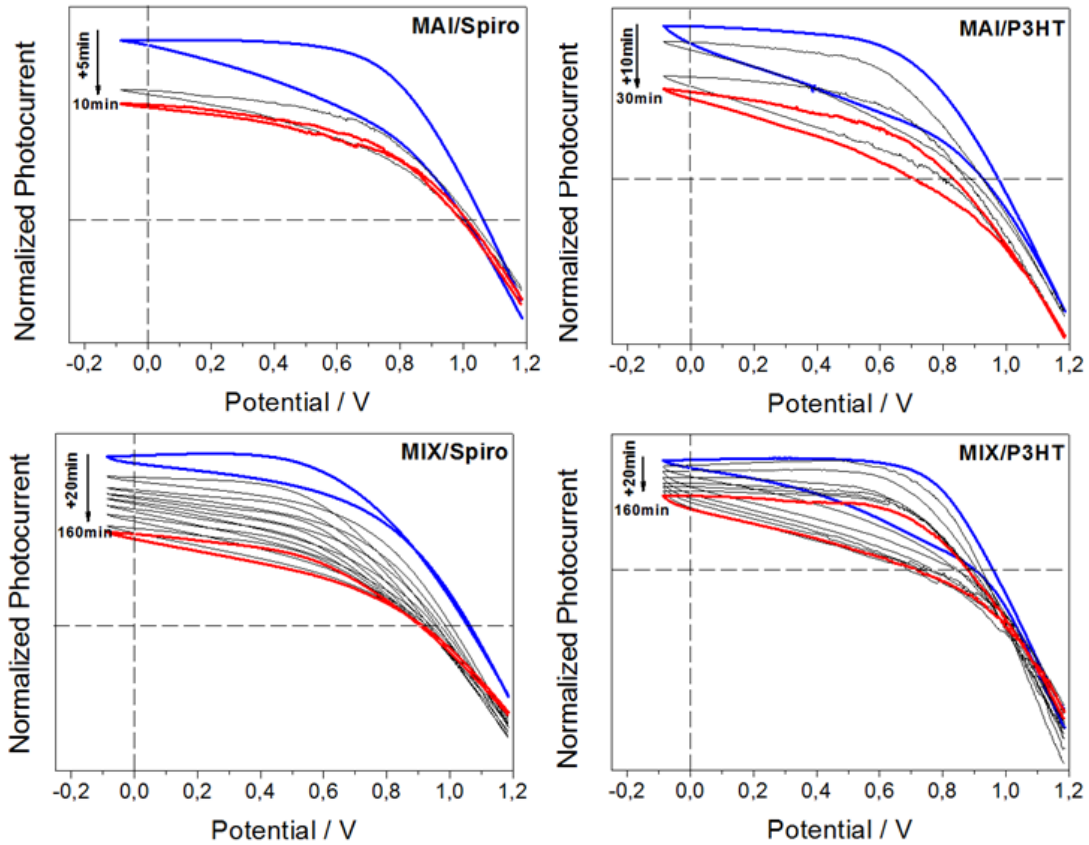
Figure 1. Normalized I-V curves for the different PSCs (blue) before and (black, red) during the moisture exposure measured in the reverse scan and forward scan (cyclic voltammetry) under light intensity of 10 mW·cm^{-2} (white LED). The measurements were performed with a scan rate of 100mV·s^{-1} at room temperature.

As shown Figure 1, moisture exposure negatively affects the photovoltaic performance of the different PSCs. Both V_{OC} and J_{SC} tend to decrease with respect to the moisture exposure time. In particular, an efficiency drop of 51% and 19% after 10 min for MAI-based devices and 60% and 42% after 160min for MIX-based devices were recorded when Spiro and P3HT were used as HSL, respectively. From these results, the following trends could be extracted. Firstly, focusing on the impact of the perovskite composition, the degradation process was faster when pure perovskite (MAI) was employed as active layer in contrast to degradation rate found for MIX perovskite. The same result was found when Spiro as well as P3HT were used as HSL. As it has been previously reported, the longer device stability obtained for MIX samples was not only due to the partial inclusion of bromine anions,[28,29] but also to the combination of MA, FA and Cs cations.[34] This combination gives rise to a more thermally and structurally stable perovskite. And secondly, in relation to the nature of the HSL, Spiro-based devices are significantly less stable than those with P3HT as HSL.

In order to cast light into the perovskite degradation kinetics obtained for the different PSCs, scanning electron microscope (SEM) was used to investigate the effect of moisture exposure on the device stability. Figure 2 shows SEM images obtained for bare perovskites and MAI/HSL films deposited on Si/cTiO$_2$/mTiO$_2$ before and after moisture exposure.
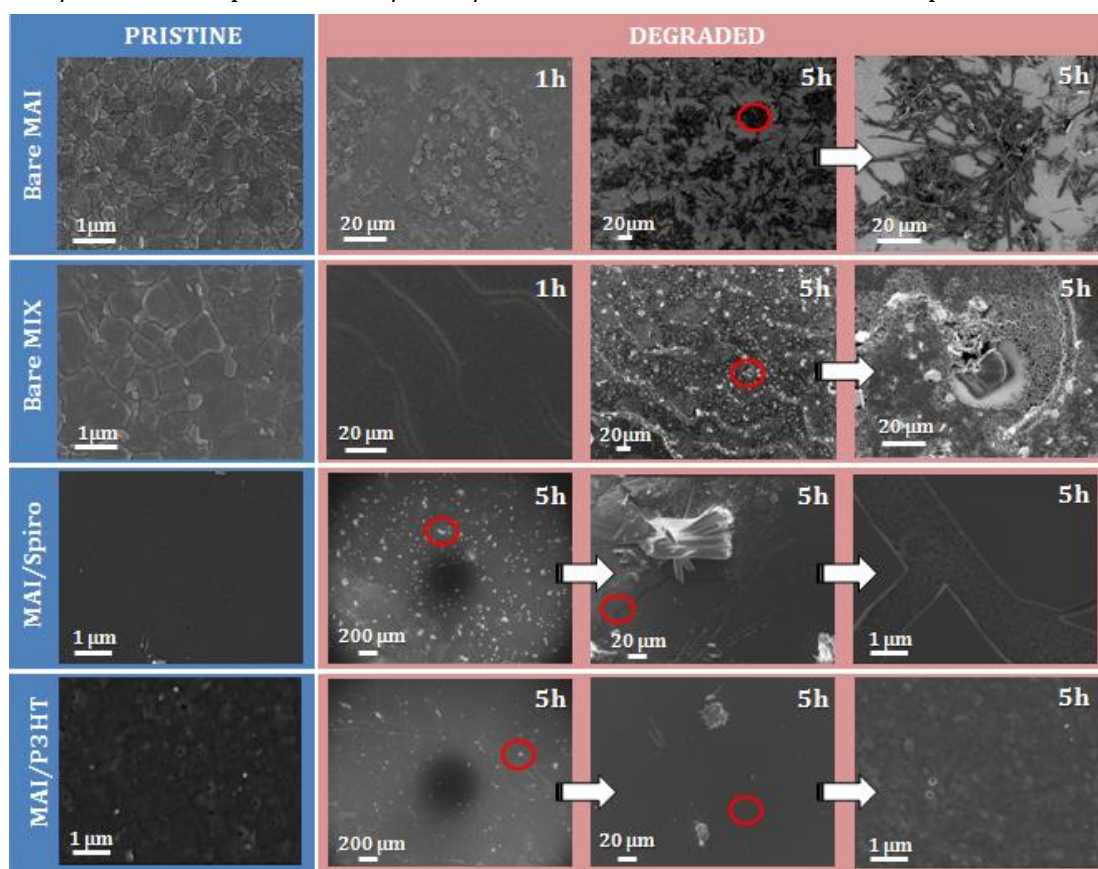

Figure 2: Plane-view scanning electron microscopy (SEM) images for the MAI, MIX, MAI/Spiro and MAI/P3HT layers after moisture exposure (RH= 90%) for 1 and 5h at room temperature.

Before moisture exposure, both uncovered perovskites layers formed homogeneous and free-pinholes films, with larger grain size for MIX perovskite. However, after moisture exposure remarkable morphological changes were observable in both cases. In the case of bare MAI layers, large perovskite crystals with well-defined faces appeared leading to extensive pin-holes after 1 hour under moisture exposure. For longer times (5 hours), larger structures with dendritic shape were formed. In contrast, as it was expected according to the literature,[28,29,34] no significant change was observed for MIX layers for at least 1 hour under moisture exposure. However, after 5 hours, large perovskite crystals with reduced pin-holes around them were produced. The formation of these large perovskite structures seems to be related to the perovskite aggregation process (Figure S3 in Supporting Information). In contrast to a previous report,[38] EDX analysis showed the same Pb/I ratio for fresh and degraded samples.

To investigate the influence of the HSL on the device stability, the most unstable perovskite (MAI) was used as active layer. As shown Figure 2, as a result of the perovskite degradation, an increased number of emerging structures coming from the underlying perovskite layer appeared when Spiro was used as HSL. These new formed crystals led even to the fracture

of the Spiro layer. In contrast, after 5 hours under moisture exposure the P3HT layer appears unchanged. This behavior can be ascribed to the hydrophobic character of P3HT layer[BMAI3],[25] which makes the penetration/percolation of water molecules towards the underlying perovskite layer more difficult. Table S2 gathers the water contact angles (WCAs) for the different configurations showing WCAs > 90º, i. e. a hydrophobic character, for the P3HT surfaces on both MAI and MIX perovskites. Similar behavior was previously reported using UV-Vis and FTIR spectroscopy.[18,39] On the other hand, Spiro devices presented hydrophilic surfaces with WCAs < 80º for MAI/Spiro and MIX/Spiro samples. Therefore, it seems reasonable to assume that the short stability obtained for MAI/Spiro devices was connected to both the perovskite decomposition process, higher affinity to water and consequent degradation of the Spiro layer.
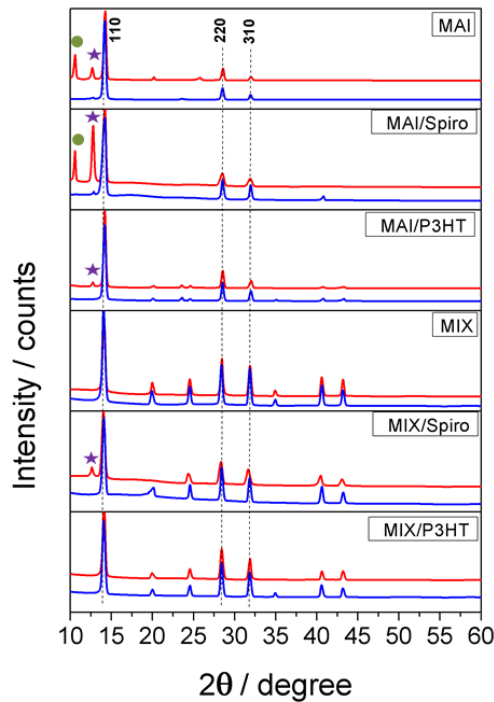

Figure 3. X-ray diffraction for the different (MAI and MIX) perovskite layers with and without the HSL (Spiro and P3HT) deposited on the top (blue line) before and (red line) after moisture exposure for 1 hour. The positions of the XRD peaks for (purple star) PbI₂ and (green circle) hydrated complex are marked in the graphs.

Figure 3 shows XRD patterns of the two perovskites (MAI and MIX) with and without HSL (Spiro and P3HT) before and after moisture exposure. The characteristic diffraction peaks of tetragonal perovskite phase (14.1°, 28.5° and 31.9°)[31,40] were obtained for fresh samples, which remained at the same position when the samples were subjected to humidity (RH > 90) for 1 hour. As it was previously reported, any additional peak appears as a consequence of HSLs. Nevertheless, additional diffraction peaks previously related to the formation of hydrated perovskite complex and PbI₂ were found after moisture exposure at 10.5° and 12.7°, respectively.[31,40–42] Focusing the attention on these two diffraction peaks, different behavior can be observed depending on the perovskite composition and/or HSL. Firstly, for uncovered perovskite layers these two peaks were only observable for MAI perovskite after moisture exposure. And secondly, contrary to what it could be expected, higher signal intensities for these two diffraction peaks were found for MAI/Spiro with respect to the

uncovered MAI sample. Similar behavior was found for MIX perovskite. In this case, the signal previously attributed to PbI_2 was only found for MIX/Spiro sample after moisture exposure, whereas it was not observed for bare MIX and MIX/P3HT samples. Therefore, the rapid degradation kinetics found for MAI/Spiro samples (Figure 1) could not only be related to the perovskite composition and/or the degradation of the Spiro (Figure 2), but also to a possible interfacial interaction of both layers.[43] We have further analyzed the chemical composition of the device by XPS for as-prepared and exposed surfaces. See Table S? [BMAI4]for the comparison of the atomic percentages of the different elements in surface (Pb, I, O, C, N, S, F and Ti). It is interesting to stress several aspects; first, after exposure of the MAI perovskite surface to humidity part of the TiO_2 interface is revealed, meanwhile MIX surface composition only varies in the relative atomic percentage without appearance of any new contribution. After exposition to humidity, a percentage below the 1% of I appears in all the surfaces except for the MIX/P3HT that only presents a slightly variation in the C and S contributions. Bearing in mind these results, the following trend can be established to define device stability: MAI/Spiro < MAI/P3HT < MIX/Spiro < MIX/P3HT. These results bring to light the importance of device engineering in the development of this technology for its outdoor application.

 Once the impact of the moisture exposure on the device stability has been assessed according to the perovskite composition and the material employed as HSL, we focus our attention on the electronic processes determining the photovoltaic performance. To study the effect of moisture exposure on the device performance, we analyze the impedance response in the form of Nyquist and frequency-dependent capacitance plots (Figure 4). At this point, it is important to remark that the different PSCs were subjected to different moisture exposure times bearing in mind the different degradation kinetics demonstrated above. Therefore, in order to safely isolate the effect of the degradation rate, a photocurrent drop of 50% was employed as criterion for the exposure time. After the moisture exposure, the PCSs were flushed with dry nitrogen for 1 hour before starting the characterization by impedance spectroscopy.
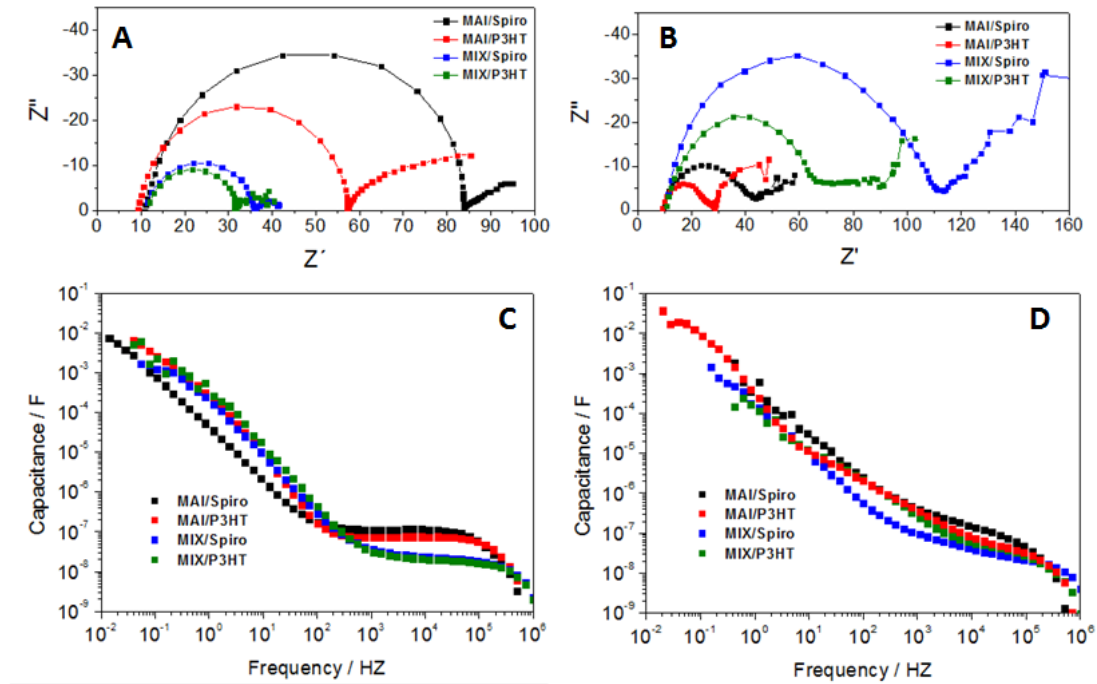
Figure 4. (A, B) Impedance spectra and (C, D) frequency-dependent capacitance obtained at open-circuit condition and under white illumination for (A, C) fresh and (B, D) degraded PSCs. The excitation illumination intensity was fixed such a photopotential close to the 1-sun V_{OC} is generated (Table S1).

As shown in Figure 4A, the impedance spectra obtained for fresh PSCs were characterized by two signals (semicircles or arcs). These two signals will only be well-detected when the peak maxima on Bode plots are sufficiently well separated (see Supporting Information, Figure S4). As it was previously reported,[44–48] the signal appearing at high frequencies (HF), the closest one to the origin and the largest semicircle, has been attributed to electronic transport/recombination processes, whereas the signal appearing at low frequencies (LF) has been related to ionic diffusion and charge accumulation at contacts. These two signals exhibit significant changes in the impedance spectra after moisture exposure. In particular, a distortion of the HF semicircle was found for degraded PSCs (Figure 4B). This behavior seems to be more remarkable for degraded P3HT-based devices. This feature could explain the non-symmetric shape of the HF peak in the Bode plots that was found for degraded PSCs (see Figure S4 in Supporting Information). The non-symmetric shape suggests that the time constant of a process previously hidden under the HF semicircle after degradation becomes now resolved or, alternatively, the appearance of a new capacitive process. The general response of the frequency-dependent capacitance for fresh and degraded devices is shown in Figure 4C and 4D, respectively. According to the literature,[44,47,49,50] each plateau is related to a certain specific polarization process. In particular, the LF plateau was attributed to accumulation of majority carriers at the TiO$_2$/perovskite interface, which seems to be related to the characteristic hysteretic behavior found in PSCs.[50,51] On the other hand, the HF plateau was associated with the dielectric polarization of the perovskite in the bulk. In accordance to the different thicknesses of the perovskite layers (d) (see Figure S5 in the Supporting Information) and the expression for the bulk capacitance $C = A\varepsilon/d$, higher HF capacitance values were found for MAI-based devices. Focusing on the effect of the moisture exposure, although the capacitance values observed for HF and LF plateaus are in the same

range ($\approx 10^{-7}$ F/cm^{-2} and $\approx 10^{-2}$ F/cm^{-2}, respectively) for fresh and degraded devices, the fact is that a new plateau in the range of 10^{-6} - 10^{-5} F/cm^{-2} was found at mid frequencies after moisture exposure. This effect seems to be more remarkable for P3HT-based devices.

A similar behavior has been previously reported for PSCs with less efficient external contacts. In particular, impedance spectra and frequency-dependent capacitance plots were characterized by the presence of an additional MF component when TiO_2 and Nb_2O_5 were employed as electron selective layer (ESL) in aged devices.[44] Guerrero and coworkers associated this characteristic feature with the charge accumulation at the ESL/perovskite interface due to the low charge extraction efficiency of these selective contacts. Additionally, an interfacial recombination enhancement was suggested as a consequence of this charge accumulation process. Nevertheless, it should be considered that this charge separation/extraction process is not only determined by the ESL, but also by the perovskite itself and the material used as HSL. As it was reported, the interfacial interactions between the selective contacts and the perovskite layer affect the energetic barriers that determine the charge separation/extraction processes.[50,52–55] Therefore, bearing in mind [BMAI5] that our devices are characterized by the same ESL, the MF component could be associated with an interfacial charge accumulation process due to the perovskite composition and material employed as HSL which can not only determine the charge extraction at the ESL/perovskite interface, but also at the perovskite/HSL interface. This interpretation could explain the difference found for Spiro and P3HT-based devices described above (Figure 4 and S4).

In order to cast light [BMAI6] into the origin of this new feature appearing at mid frequencies after moisture exposure, impedance spectroscopy was measured using two different illumination wavelengths to modify the charge generation profile inside the perovskite layer. Bearing in mind the absorption spectra widely reported in the literature and taking into account the Lambert-Beer Law, a different spatial penetration of the optical excitation inside the perovskite layer is expected for blue and red illumination. Photogenerated charge would show a concentration gradient governed by the absorption coefficient.[56] In particular, a higher concentration of photogenerated charge would be expected at the ESL/perovskite interface than at the perovskite/HSL one under blue illumination. In contrast, the profile of photogenerated charge is more uniform under red illumination. A similar methodology was previously used to analyze the recombination processes.[57] **COLOR PAPER**
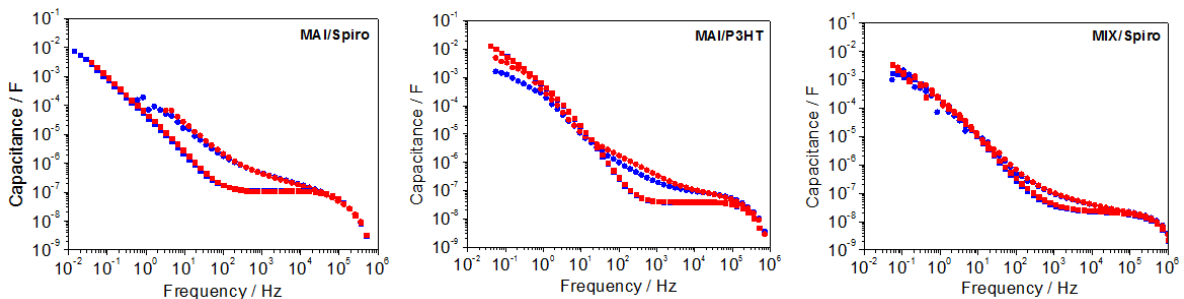

Figure 5. Frequency-dependent capacitance obtained at open-circuit condition and under illumination for (squares) fresh and (circles) degraded MAI/Spiro, MAI/P3HT and MIX/Spiro devices using the two excitation wavelengths of (blue) λ_{blue} = 465 nm and (red) λ_{red} = 635 nm.

Figure 5 shows the capacitance-frequency response under blue and red illumination for MAI/Spiro, MAI/P3HT and MIX/Spiro devices before and after moisture exposure. In line with Figures 4C and 4D, the capacitance-frequency response obtained under blue and red illumination was characterized by the presence of a characteristic plateau appearing at mid frequencies (10^4–10^2 Hz) which overlaps with the HF plateau (bulk capacitance) after moisture exposure. For fresh devices the capacitance-frequency response was not affected by electron-hole generation profile produced as a result of the different optical excitation wavelengths employed during the impedance spectroscopy. A similar behavior was found for degraded MAI/Spiro and MIX/Spiro devices. In contrast, a significant difference was found at mid frequencies for degraded MAI/P3HT devices when the electron-hole generation profile was modified. In particular, higher MF capacitance values were found when the availability of the photogenerated charges was higher at the perovskite/HSL interface (red illumination) with respect to when charge was photogenerated preferentially in the vicinity of the ESL (blue illumination). This behavior is also brought to light in the Nyquist plots by the presence of the MF semicircle for degraded MAI/P3HT devices under red illumination (see Supporting Information, Figure S6). Therefore, a more important interfacial charge accumulation process seems to take place after moisture exposure when P3HT was used as HSL and, consequently, a poorer hole extraction is expected at the perovskite/P3HT interface with respect to perovskite/Spiro. This possible interpretation could not only explain the distorted HF semicircle and/or the apparent MF semicircle found in Nyquist plot of impedance spectra for degraded devices, respectively (Figure 4B and Figure S6), but also the more remarkable MF capacitance plateau observed for P3HT-based devices (Figure 4D). On the other hand, as it was mentioned above, the energetic barriers that determine the charge extraction/separation process is also depending on the perovskite material. As shown in Figure 5C, when the Spiro was used as HSL the capacitance-frequency response obtained under blue and red illumination shows the same behavior before and after moisture exposure. Similar results were found for MAI/Spiro devices (Figure 5A). Nevertheless, this MF capacitance plateau seems to be less visible after moisture exposure which suggest a better electron and hole extraction in both interfaces even after moisture exposure. This robustness of the electronic properties of the Spiro contact explains the normally better photocurrents obtained in devices when this material is used.

In order to understand the differences found in the Nyquist plot of impedance spectra under different optical excitation wavelengths for degraded devices (see Supporting Information, Figure S6), the recombination (HF) kinetics was investigated. Figure 6 shows the electron recombination resistance extracted by fitting the impedance response under blue and red illumination for fresh and degraded MAI/Spiro devices to a simple -R_{Ser}-(R_{LF},CPE_1)-(R_{HF},CPE_2)- equivalent circuit. To be sure about the fitting, the time constant (τ) were estimated as (1) $\tau=R_{rec}\cdot C_b$, where R_{rec} is the electron (HF) recombination resistance and C_b is the bulk capacitance; and (2) $\tau=1/2\pi f$, where f is the frequency peak maximum directly extracted from Bode plots. The same behavior was found for both fresh and degraded devices (see Supporting Information, Figure S7).
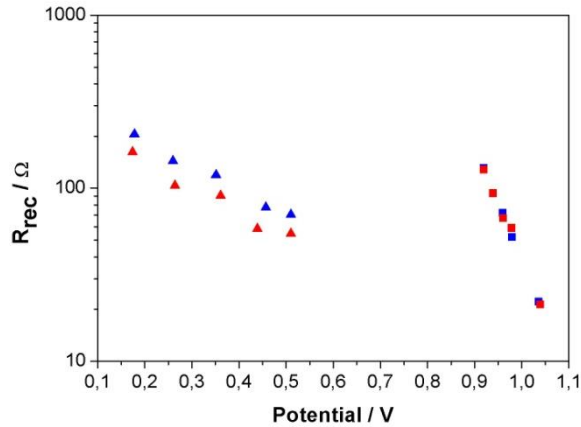
Figure 6. Recombination (HF) resistance versus open-circuit potential as extracted from fittings of the impedance spectra using the two excitation wavelengths of (blue) λ_{blue} = 465 nm and (red) λ_{red} = 635 nm for (squares) fresh and (triangles) degraded MAI/Spiro device.

In particular, the recombination resistance shows the same behavior for fresh devices regardless of the electron-hole generation profile. In contrast, a small difference was found after moisture exposure when the optical excitation wavelength was changed. For degraded devices, smaller values of electron recombination resistance were found when the red illumination was used as optical excitation. In other words, the photogenerated charge at the perovskite/HSL interface seems to recombine strongly than the photogenerated charge at the ESL/perovskite interface for a degraded device. On the other hand, a remarkable change of the slope of the recombination resistance for both optical excitations was observed with respect to fresh devices. Similar results were obtained for all devices when a white LED was employed as illumination source before and after moisture exposure (see Supporting Information, Figure S8). This observation suggests that the charge that has been mainly photogenerated at the ESL/perovskite and perovskite/HSL interface are subjected to different recombination mechanisms after moisture exposure. As it was previously reported by us, **COLOR PAPER** the results obtained for fresh devices suggest that the main recombination process is mediated via a trap-limited mechanism in the bulk of the perovskite.[58–61] However, superficial recombination could be more important as a consequence of the perovskite degradation by the moisture.[40,62,63] Therefore, the increase of this surface-mediated recombination seems to be intimately related to the larger interfacial charge accumulation described above (Figure 5). Similar results were expected for the rest of devices studied in this work as revealed by Nyquist and Bode plots obtained under both optical excitations showing the same behavior (see Supporting Information, Figure S6 and Figure S9, respectively).

This interpretation seems to be in line with the conclusions previously reported by A. Leguy and coworkers.[40] In particular, they related the efficiency drop after moisture exposure to the isolation of the perovskite grains which would reduce the charge transport leading to an increased recombination at the grain interfaces. In other words, the grain insulating effect could limit the charge transport and improve the charge recombination giving rise to shorter charge diffusion lengths.[62,63] In order to consolidate this assumption, IMPS was measured to provide information about the different charge transport processes (Figure 7).
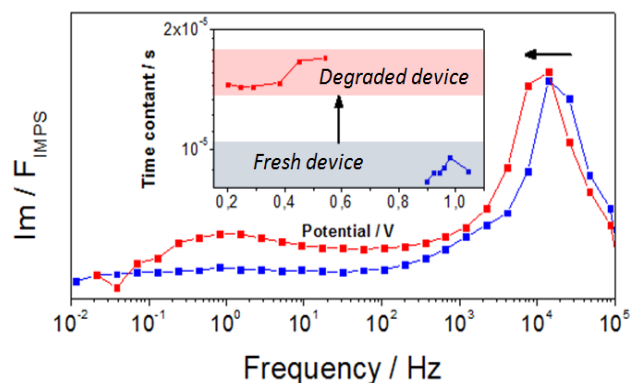
Figure 7. IMPS frequency plot of the imaginary part for MAI/Spiro device (blue) before and (red) after moisture exposure obtained under white illumination.

As ~~shown~~presented in Figure 7, IMPS frequency plot shows two well differentiated peaks with respect to the frequency scale which have been previously related to different charge transport processes characterized by different time constants.[45,51,64] In particular, the HF peak ($\approx 10^4$ Hz) was associated with the electron transport inside perovskite layer, whereas the LF peak (≈ 1 Hz) was attributed to ionic motion. In addition, a peak at mid frequencies was also found and related to the electron transport process in the mesoporous TiO_2 matrix.[51,64] Nevertheless, this MF peak was not resolved in our case (Figure 7). Paying attention to the HF peak only, a lower charge diffusion coefficient (Dn) is expected for degraded devices, since the HF peak appears at lower frequencies ($Dn= L_d^2/\tau_{HF}$, where L_d is the thickness of the perovskite layer and τ_{HF} is the HF time constant).[65] A smaller diffusion coefficient gives rise to shorter charge diffusion lengths, in line with the faster recombination observed in the degraded samples.

CONCLUSIONS

We have investigated the effect of the moisture-induced degradation of perovskite solar cells using a combination of materials characterization techniques (SEM, EDX, XRD and XPS) and small-perturbation optoelectronic techniques (impedance and intensity modulated photocurrent spectroscopies). We studied the influence of the perovskite composition and material employed as HSL on the device stability. In particular, our results reveal a lower degradation rate for perovskite solar cells based on ($Cs_{0.05}(MAPbBr_3)_{0.15}(FAPbI_3)_{0.85}$) as active layer and P3HT as HSL. On the other hand, the effect of the moisture-induced degradation on the electronic processes that determine the photovoltaic performance in perovskite solar cell was also investigated. Regardless of the device configuration, the charge recombination is governed by the bulk of the perovskite layer via a trap-limited mechanism. However, the moisture-induced degradation modifies the charge recombination mechanism. The additional mid-frequency component recorded in both Nyquist and Bode plots after moisture exposure suggests an interfacial charge accumulation. This charge accumulation process can accelerate the charge recombination rate due to a greater contribution of a surface-mediated recombination route. Additionally, a slower electron transport in perovskite layers was also evidenced in the results, which can

be traced back to the formation of more grain boundaries as a consequence of the moisture-induced degradation.

REFERENCES

(1) Xing, G.; Mathews, N.; Sun, S.; Lim, S. S.; Lam, Y. M.; Grätzel, M.; Mhaisalkar, S.; Sum, T. C. Long-Range Balanced Electron- and Hole-Transport Lengths in Organic-Inorganic CH3NH3PbI3. *Science* **2013**, *342* (6156), 344–347.

(2) Stranks, S. D.; Eperon, G. E.; Grancini, G.; Menelaou, C.; Alcocer, M. J. P.; Leijtens, T.; Herz, L. M.; Petrozza, A.; Snaith, H. J. Electron-Hole Diffusion Lengths Exceeding 1 Micrometer in an Organometal Trihalide Perovskite Absorber. *Science* **2013**, *342* (6156), 341–344.

(3) Tress, W.; Marinova, N.; Inganäs, O.; Nazeeruddin, M. K.; Zakeeruddin, S. M.; Graetzel, M. Predicting the Open-Circuit Voltage of CH3NH3PbI3 Perovskite Solar Cells Using Electroluminescence and Photovoltaic Quantum Efficiency Spectra: The Role of Radiative and Non-Radiative Recombination. *Adv. Energy Mater.* **2015**, *5* (3), n/a-n/a.

(4) Pellet, N.; Gao, P.; Gregori, G.; Yang, T.-Y.; Nazeeruddin, M. K.; Maier, J.; Grätzel, M. Mixed-Organic-Cation Perovskite Photovoltaics for Enhanced Solar-Light Harvesting. *Angew. Chem. Int. Ed.* **2014**, *53* (12), 3151–3157.

(5) Ogomi, Y.; Morita, A.; Tsukamoto, S.; Saitho, T.; Fujikawa, N.; Shen, Q.; Toyoda, T.; Yoshino, K.; Pandey, S. S.; Ma, T.; et al. CH3NH3SnxPb(1–x)I3 Perovskite Solar Cells Covering up to 1060 Nm. *J. Phys. Chem. Lett.* **2014**, *5* (6), 1004–1011.

(6) Kojima, A.; Teshima, K.; Shirai, Y.; Miyasaka, T. Novel Photoelectrochemical Cell with Mesoscopic Electrodes Sensitized by Lead-Halide Compounds (5). *Meet. Abstr.* **2007**, *MA2007-02* (8), 352–352.

(7) Photovoltaic Research | NREL https://www.nrel.gov/pv/ (accessed Feb 10, 2017).

(8) Ball, J. M.; Lee, M. M.; Hey, A.; Snaith, H. Low-Temperature Processed Mesosuperstructured to Thin-Film Perovskite Solar Cells. *Energy Environ. Sci.* **2013**.

(9) Zhou, H.; Chen, Q.; Li, G.; Luo, S.; Song, T.; Duan, H.-S.; Hong, Z.; You, J.; Liu, Y.; Yang, Y. Interface Engineering of Highly Efficient Perovskite Solar Cells. *Science* **2014**, *345* (6196), 542–546.

(10) Burschka, J.; Pellet, N.; Moon, S.-J.; Humphry-Baker, R.; Gao, P.; Nazeeruddin, M. K.; Grätzel, M. Sequential Deposition as a Route to High-Performance Perovskite-Sensitized Solar Cells. *Nature* **2013**, *499* (7458), 316–319.

(11) Liu, M.; Johnston, M. B.; Snaith, H. J. Efficient Planar Heterojunction Perovskite Solar Cells by Vapour Deposition. *Nature* **2013**, *501* (7467), 395–398.

(12) Jeon, N. J.; Noh, J. H.; Kim, Y. C.; Yang, W. S.; Ryu, S.; Seok, S. I. Solvent Engineering for High-Performance Inorganic–organic Hybrid Perovskite Solar Cells. *Nat Mater* **2014**, *13* (9), 897–903.

(13) Reyna, Y.; Salado, M.; Kazim, S.; Pérez-Tomas, A.; Ahmad, S.; Lira-Cantu, M. Performance and Stability of Mixed FAPbI3(0.85)MAPbBr3(0.15) Halide Perovskite Solar Cells under Outdoor Conditions and the Effect of Low Light Irradiation. *Nano Energy* **2016**, *30*, 570–579.

(14) Li, B.; Li, Y.; Zheng, C.; Gao, D.; Huang, W. Advancements in the Stability of Perovskite Solar Cells: Degradation Mechanisms and Improvement Approaches. *RSC Adv.* **2016**, *6* (44), 38079–38091.

(15) Wang, Z.; Shi, Z.; Li, T.; Chen, Y.; Huang, W. Stability of Perovskite Solar Cells: A Prospective on the Substitution of the A Cation and X Anion. *Angew. Chem. Int. Ed.* **2017**, *56* (5), 1190–1212.

(16) Berhe, T. A.; Su, W.-N.; Chen, C.-H.; Pan, C.-J.; Cheng, J.-H.; Chen, H.-M.; Tsai, M.-C.; Chen, L.-Y.; Dubale, A. A.; Hwang, B.-J. Organometal Halide Perovskite Solar Cells: Degradation and Stability. *Energy Environ. Sci.* **2016**, *9* (2), 323–356.

(17) Niu, G.; Li, W.; Meng, F.; Wang, L.; Dong, H.; Qiu, Y. Study on the Stability of CH3NH3PbI3 Films and the Effect of Post-Modification by Aluminum Oxide in All-Solid-State Hybrid Solar Cells. *J Mater Chem A* **2014**, *2* (3), 705–710.

(18) Yang, J.; Siempelkamp, B. D.; Liu, D.; Kelly, T. L. Investigation of CH3NH3PbI3 Degradation Rates and Mechanisms in Controlled Humidity Environments Using in Situ Techniques. *ACS Nano* **2015**, *9* (2), 1955–1963.

(19) Bryant, D.; Aristidou, N.; Pont, S.; Sanchez-Molina, I.; Chotchunangatchaval, T.; Wheeler, S.; Durrant, J. R.; Haque, S. A. Light and Oxygen Induced Degradation Limits the Operational Stability of Methylammonium Lead Triiodide Perovskite Solar Cells. *Energy Environ. Sci.* **2016**, *9* (5), 1655–1660.

(20) Kang, S. M.; Ahn, N.; Lee, J.-W.; Choi, M.; Park, N.-G. Water-Repellent Perovskite Solar Cell. *J. Mater. Chem. A* **2014**, *2* (47), 20017–20021.

(21) Guarnera, S.; Abate, A.; Zhang, W.; Foster, J. M.; Richardson, G.; Petrozza, A.; Snaith, H. J. Improving the Long-Term Stability of Perovskite Solar Cells with a Porous Al2O3 Buffer Layer. *J. Phys. Chem. Lett.* **2015**, *6* (3), 432–437.

(22) Zheng, L.; Chung, Y.-H.; Ma, Y.; Zhang, L.; Xiao, L.; Chen, Z.; Wang, S.; Qu, B.; Gong, Q. A Hydrophobic Hole Transporting Oligothiophene for Planar Perovskite Solar Cells with Improved Stability. *Chem. Commun.* **2014**, *50* (76), 11196–11199.

(23) Hwang, I.; Jeong, I.; Lee, J.; Ko, M. J.; Yong, K. Enhancing Stability of Perovskite Solar Cells to Moisture by the Facile Hydrophobic Passivation. *ACS Appl. Mater. Interfaces* **2015**, *7* (31), 17330–17336.

(24) Bella, F.; Griffini, G.; Correa-Baena, J.-P.; Saracco, G.; Grätzel, M.; Hagfeldt, A.; Turri, S.; Gerbaldi, C. Improving Efficiency and Stability of Perovskite Solar Cells with Photocurable Fluoropolymers. *Science* **2016**.

(25) Kwon, Y. S.; Lim, J.; Yun, H.-J.; Kim, Y.-H.; Park, T. A Diketopyrrolopyrrole-Containing Hole Transporting Conjugated Polymer for Use in Efficient Stable Organic-Inorganic Hybrid Solar Cells Based on a Perovskite. *Energy Environ. Sci.* **2014**, *7* (4), 1454–1460.

(26) Green, M. A.; Ho-Baillie, A.; Snaith, H. J. The Emergence of Perovskite Solar Cells. *Nat Photon* **2014**, *8* (7), 506–514.

(27) Amat, A.; Mosconi, E.; Ronca, E.; Quarti, C.; Umari, P.; Nazeeruddin, M. K.; Grätzel, M.; De Angelis, F. Cation-Induced Band-Gap Tuning in Organohalide Perovskites: Interplay of Spin–Orbit Coupling and Octahedra Tilting. *Nano Lett.* **2014**, *14* (6), 3608–3616.

(28) Noh, J. H.; Im, S. H.; Heo, J. H.; Mandal, T. N.; Seok, S. I. Chemical Management for Colorful, Efficient, and Stable Inorganic–Organic Hybrid Nanostructured Solar Cells. *Nano Lett.* **2013**, *13* (4), 1764–1769.

(29) Misra, R. K.; Aharon, S.; Li, B.; Mogilyansky, D.; Visoly-Fisher, I.; Etgar, L.; Katz, E. A. Temperature- and Component-Dependent Degradation of Perovskite Photovoltaic Materials under Concentrated Sunlight. *J. Phys. Chem. Lett.* **2015**, *6* (3), 326–330.

(30) Poglitsch, A.; Weber, D. Dynamic Disorder in Methylammoniumtrihalogenoplumbates (II) Observed by Millimeter-wave Spectroscopy. *J. Chem. Phys.* **1987**, *87* (11), 6373–6378.

(31) Petrus, M. L.; Hu, Y.; Moia, D.; Calado, P.; Leguy, A. M. A.; Barnes, P. R. F.; Docampo, P. The Influence of Water Vapor on the Stability and Processing of Hybrid Perovskite Solar Cells Made from Non-Stoichiometric Precursor Mixtures. *ChemSusChem* **2016**, *9* (18), 2699–2707.

(32) Zhao, Y.; Zhu, K. Organic-Inorganic Hybrid Lead Halide Perovskites for Optoelectronic and Electronic Applications. *Chem. Soc. Rev.* **2016**, *45* (3), 655–689.

(33) Sutton, R. J.; Eperon, G. E.; Miranda, L.; Parrott, E. S.; Kamino, B. A.; Patel, J. B.; Hörantner, M. T.; Johnston, M. B.; Haghighirad, A. A.; Moore, D. T.; et al. Bandgap-Tunable Cesium Lead Halide Perovskites with High Thermal Stability for Efficient Solar Cells. *Adv. Energy Mater.* **2016**, *6* (8), 1502458–n/a.

(34) Saliba, M.; Matsui, T.; Seo, J.-Y.; Domanski, K.; Correa-Baena, J.-P.; Nazeeruddin, M. K.; Zakeeruddin, S. M.; Tress, W.; Abate, A.; Hagfeldt, A.; et al. Cesium-Containing Triple Cation Perovskite Solar Cells: Improved Stability, Reproducibility and High Efficiency. *Energy Environ. Sci.* **2016**, *9* (6), 1989–1997.

(35) Bi, D.; Yang, L.; Boschloo, G.; Hagfeldt, A.; Johansson, E. M. J. Effect of Different Hole Transport Materials on Recombination in CH3NH3PbI3 Perovskite-Sensitized Mesoscopic Solar Cells. *J. Phys. Chem. Lett.* **2013**, *4* (9), 1532–1536.

(36) Jeon, N. J.; Noh, J. H.; Yang, W. S.; Kim, Y. C.; Ryu, S.; Seo, J.; Seok, S. I. Compositional Engineering of Perovskite Materials for High-Performance Solar Cells. *Nature* **2015**, *517* (7535), 476–480.

(37) Salado, M.; Idigoras, J.; Calio, L.; Kazim, S.; Nazeeruddin, M. K.; Anta, J. A.; Ahmad, S. Interface Play between Perovskite and Hole Selective Layer on the Performance and Stability of Perovskite Solar Cells. *ACS Appl. Mater. Interfaces* **2016**, *8* (50), 34414–34421.

(38) Aristidou, N.; Sanchez-Molina, I.; Chotchuangchutchaval, T.; Brown, M.; Martinez, L.; Rath, T.; Haque, S. A. The Role of Oxygen in the Degradation of Methylammonium Lead Trihalide Perovskite Photoactive Layers. *Angew. Chem. Int. Ed.* **2015**, *54* (28), 8208–8212.

(39) Idigoras, J.; Todinova, A.; Sanchez-Valencia, J. R.; Barranco, A.; Borras, A.; Anta, J. A. The Interaction between Hybrid Organic-Inorganic Halide Perovskite and Selective Contacts in Perovskite Solar Cells: An Infrared Spectroscopy Study. *Phys Chem Chem Phys* **2016**, *18* (19), 13583–13590.

(40) Leguy, A. M. A.; Hu, Y.; Campoy-Quiles, M.; Alonso, M. I.; Weber, O. J.; Azarhoosh, P.; van Schilfgaarde, M.; Weller, M. T.; Bein, T.; Nelson, J.; et al. Reversible Hydration of CH3NH3PbI3 in Films, Single Crystals, and Solar Cells. *Chem. Mater.* **2015**, *27* (9), 3397–3407.

(41) Guo, X.; McCleese, C.; Kolodziej, C.; Samia, A. C. S.; Zhao, Y.; Burda, C. Identification and Characterization of the Intermediate Phase in Hybrid Organic-Inorganic MAPbI3 Perovskite. *Dalton Trans.* **2016**, *45* (9), 3806–3813.

(42) Guo, X.; McCleese, C.; Lin, W.-C.; Burda, C. Curing of Degraded MAPbI3 Perovskite Films. *RSC Adv.* **2016**, *6* (65), 60620–60625.

(43) Carrillo, J.; Guerrero, A.; Rahimnejad, S.; Almora, O.; Zarazua, I.; Mas-Marza, E.; Bisquert, J.; Garcia-Belmonte, G. Ionic Reactivity at Contacts and Aging of Methylammonium Lead Triiodide Perovskite Solar Cells. *Adv. Energy Mater.* **2016**, *6* (9), 1502246–n/a.

(44) Guerrero, A.; Garcia-Belmonte, G.; Mora-Sero, I.; Bisquert, J.; Kang, Y. S.; Jacobsson, T. J.; Correa-Baena, J.-P.; Hagfeldt, A. Properties of Contact and Bulk Impedances in Hybrid Lead Halide Perovskite Solar Cells Including Inductive Loop Elements. *J. Phys. Chem. C* **2016**, *120* (15), 8023–8032.

(45) Guillén, E.; Ramos, F. J.; Anta, J. A.; Ahmad, S. Elucidating Transport-Recombination Mechanisms in Perovskite Solar Cells by Small-Perturbation Techniques. *J. Phys. Chem. C* **2014**, *118* (40), 22913–22922.

(46) Todinova, A.; Idígoras, J.; Salado, M.; Kazim, S.; Anta, J. A. Universal Features of Electron Dynamics in Solar Cells with TiO2 Contact: From Dye Solar Cells to Perovskite Solar Cells. *J. Phys. Chem. Lett.* **2015**, *6* (19), 3923–3930.

(47) Bag, M.; Renna, L. A.; Adhikari, R. Y.; Karak, S.; Liu, F.; Lahti, P. M.; Russell, T. P.; Tuominen, M. T.; Venkataraman, D. Kinetics of Ion Transport in Perovskite Active Layers and Its Implications for Active Layer Stability. *J. Am. Chem. Soc.* **2015**, *137* (40), 13130–13137.

(48) Dualeh, A.; Moehl, T.; Tétreault, N.; Teuscher, J.; Gao, P.; Nazeeruddin, M. K.; Grätzel, M. Impedance Spectroscopic Analysis of Lead Iodide Perovskite-Sensitized Solid-State Solar Cells. *ACS Nano* **2014**, *8* (1), 362–373.

(49) Kim, H.-S.; Jang, I.-H.; Ahn, N.; Choi, M.; Guerrero, A.; Bisquert, J.; Park, N.-G. Control of I–V Hysteresis in CH3NH3PbI3 Perovskite Solar Cell. *J. Phys. Chem. Lett.* **2015**, *6* (22), 4633–4639.

(50) Zarazua, I.; Bisquert, J.; Garcia-Belmonte, G. Light-Induced Space-Charge Accumulation Zone as Photovoltaic Mechanism in Perovskite Solar Cells. *J. Phys. Chem. Lett.* **2016**, *7* (3), 525–528.

(51) Contreras, L.; Idigoras, J.; Todinova, A.; Salado, M.; Kazim, S.; Ahmad, S.; Anta, J. A. Specific Cation Interactions as the Cause of Slow Dynamics and Hysteresis in Dye and Perovskite Solar Cells: A Small-Perturbation Study. *Phys. Chem. Chem. Phys.* **2016**, *18* (45), 31033–31042.

(52) Habisreutinger, S. N.; Leijtens, T.; Eperon, G. E.; Stranks, S. D.; Nicholas, R. J.; Snaith, H. J. Enhanced Hole Extraction in Perovskite Solar Cells Through Carbon Nanotubes. *J. Phys. Chem. Lett.* **2014**, *5* (23), 4207–4212.

(53) Correa Baena, J. P.; Steier, L.; Tress, W.; Saliba, M.; Neutzner, S.; Matsui, T.; Giordano, F.; Jacobsson, T. J.; Srimath Kandada, A. R.; Zakeeruddin, S. M.; et al. Highly Efficient Planar Perovskite Solar Cells through Band Alignment Engineering. *Energy Environ. Sci.* **2015**, *8* (10), 2928–2934.

(54) Pydzińska, K.; Karolczak, J.; Kosta, I.; Tena-Zaera, R.; Todinova, A.; Idígoras, J.; Anta, J. A.; Ziółek, M. Determination of Interfacial Charge-Transfer Rate Constants in Perovskite Solar Cells. *ChemSusChem* **2016**, *9* (13), 1647–1659.

(55) Zou, Y.; Holmes, R. J. Temperature-Dependent Bias Poling and Hysteresis in Planar Organo-Metal Halide Perovskite Photovoltaic Cells. *Adv. Energy Mater.* **2016**, *6* (7).

(56) Yang, Y.; Yang, M.; Moore, D. T.; Yan, Y.; Miller, E. M.; Zhu, K.; Beard, M. C. Top and Bottom Surfaces Limit Carrier Lifetime in Lead Iodide Perovskite Films. *Nat. Energy* **2017**, *2*, 16207.

(57) Bi, D.; Tress, W.; Dar, M. I.; Gao, P.; Luo, J.; Renevier, C.; Schenk, K.; Abate, A.; Giordano, F.; Correa Baena, J.-P.; et al. Efficient Luminescent Solar Cells Based on Tailored Mixed-Cation Perovskites. *Sci. Adv.* **2016**, *2* (1).

(58) Wehrenfennig, C.; Liu, M.; Snaith, H. J.; Johnston, M. B.; Herz, L. M. Charge-Carrier Dynamics in Vapour-Deposited Films of the Organolead Halide Perovskite CH3NH3PbI3-xClx. *Energy Environ. Sci.* **2014**, *7* (7), 2269–2275.

(59) Manser, J. S.; Kamat, P. V. Band Filling with Free Charge Carriers in Organometal Halide Perovskites. *Nat Photon* **2014**, *8* (9), 737–743.

(60) Yang, Y.; Yang, M.; Li, Z.; Crisp, R.; Zhu, K.; Beard, M. C. Comparison of Recombination Dynamics in CH3NH3PbBr3 and CH3NH3PbI3 Perovskite Films: Influence of Exciton Binding Energy. *J. Phys. Chem. Lett.* **2015**, *6* (23), 4688–4692.

(61) Rehman, W.; Milot, R. L.; Eperon, G. E.; Wehrenfennig, C.; Boland, J. L.; Snaith, H. J.; Johnston, M. B.; Herz, L. M. Charge-Carrier Dynamics and Mobilities in Formamidinium Lead Mixed-Halide Perovskites. *Adv. Mater.* **2015**, *27* (48), 7938–7944.

(62) Li, D.; Bretschneider, S. A.; Bergmann, V. W.; Hermes, I. M.; Mars, J.; Klasen, A.; Lu, H.; Tremel, W.; Mezger, M.; Butt, H.-J.; et al. Humidity-Induced Grain Boundaries in MAPbI3 Perovskite Films. *J. Phys. Chem. C* **2016**, *120* (12), 6363–6368.

(63) Nie, W.; Tsai, H.; Asadpour, R.; Blancon, J.-C.; Neukirch, A. J.; Gupta, G.; Crochet, J. J.; Chhowalla, M.; Tretiak, S.; Alam, M. A.; et al. High-Efficiency Solution-Processed Perovskite Solar Cells with Millimeter-Scale Grains. *Science* **2015**, *347* (6221), 522.

(64) Correa-Baena, J.-P.; Anaya, M.; Lozano, G.; Tress, W.; Domanski, K.; Saliba, M.; Matsui, T.; Jacobsson, T. J.; Calvo, M. E.; Abate, A.; et al. Unbroken Perovskite: Interplay of Morphology, Electro-Optical Properties, and Ionic Movement. *Adv. Mater.* **2016**, n/a-n/a.

(65) Fabregat-Santiago, F.; Garcia-Belmonte, G.; Mora-Seró, I.; Bisquert, J. Characterization of Nanostructured Hybrid and Organic Solar Cells by Impedance Spectroscopy. *Phys. Chem. Chem. Phys.* **2011**, *13* (20), 9083–9118.